INORGANIC CHEMISTRY FRONTIERS

RESEARCH ARTICLE

View Article Online
View Journal | View Issue

Check for updates

Cite this: *Inorg. Chem. Front.*, 2023, **10**, 6588

Subtly regulating layered tin chalcogenide frameworks for optimized photo-induced carrier separation†

Chaozhuang Xue, *[a] Rui Li,[a] Wenhui Chen,[a] Yingying Zhang,[b] Ningning Zhang,*[a] Konggang Qu, [a] Ruiqing Li[c] and Huajun Yang*[b]

Received 25th July 2023,
Accepted 12th September 2023

DOI: 10.1039/d3qi01439h

rsc.li/frontiers-inorganic

Layered tin chalcogenide frameworks (LTCFs) have attracted great attention due to the stable structure and effective integration of porosity with semiconducting properties. Though they have a much suitable band gap and rich structures, the significance of LTCFs in photoelectrochemical applications and "structure–property" studies is highly undervalued. Herein, we report an example of "structure–property" correlations in photoelectrochemical applications using three subtly regulated LTCFs that show nuances in the intralayer architecture and packing mode of layers. Of particular interest is the huge difference in their photoelectric responses despite the same secondary building block (Sn_3S_4), linkers (shared Sn_2S_2) and 2D honeycomb-type topology. In particular, LTCF-3 has the highest photocurrent density, which is nearly five times that of LTCF-2. Enhanced photoelectric response for LTCF-3 was attributed to the elongated distance between adjacent clusters, which dramatically decreased the recombination of photo-induced carriers. This deduction was supported by precise structure analysis, UV-vis absorption spectroscopy and theoretical calculations.

Published on 15 9 2023. Downloaded on 2025-11-07 2:44:00.

Introduction

Crystalline chalcogenide frameworks with uniform cavities and semiconducting characteristics have gained enormous interest in the past decade because of their potential applications in photovoltaics, photocatalysis, host–guest chemistry, photoluminescence, *etc.*[1–6] The diverse molecular cluster nodes can be connected through adjustable inorganic or/and organic linkers, endowing this emerging material with infinite architecture models in theory, especially when considering the flexible bonding angles of chalcogen–metal–chalcogen.[7–11] The multiformity of structural systems and continuous structural variation make the chalcogenide framework ideal platform for establishing the "structure–function" correlations, which conversely guide structure manipulation and further property optimization. Among the various chalcogenide frameworks, three-dimensional (3D) porous chalcogenide frameworks with intricate channels and pores exhibit superior structural properties to two-dimensional (2D) frameworks, the crystalline bulk phase of which is composed of 2D layered structures. Great effort has been made in designing new 3D structures and exploring their potential applications.[4,12–16] However, recent research studies have demonstrated that 2D chalcogenide frameworks have the advantages of structural regulation, functional optimization and structural stability. Till date, only a few cluster-based 3D chalcogenide frameworks (*e.g.*, UCR-20, CPM-120, and ITF-9) exhibit robust structures and accessible channels or cavities, which to a great extent limit the development and application of 3D chalcogenides in various fields.[17–19] By contrast, the robust layered chalcogenides can be readily obtained and are widely used in various fields.[20–23]

2D chalcogenide frameworks can be appropriately synthesized by introducing high-valence metal cations to interrupt the extension from high-dimension direction, and meanwhile reduce the size and charge density of clusters.[24–26] As a result, the 2D chalcogenide frameworks obtained *via* this strategy usually have simple as well as stable structures, allowing the intensive investigation in photoelectrochemistry and host–guest chemistry by means of intrinsic semiconducting properties and structural characteristics such as large interspace between adjacent layers and small inerratic channels perpen-

[a]*School of Chemistry and Chemical Engineering, Liaocheng University, Liaocheng, 252059, China. E-mail: czxuelc@163.com, zhangningning@lcu.edu.cn*
[b]*School of Chemistry and Materials Science, Nanjing Normal University, 210023 Nanjing, China. E-mail: huajunyang@nnu.edu.cn*
[c]*School of Textile and Clothing, Nantong University, Nantong 226019, China*

†Electronic supplementary information (ESI) available: Additional figures, powder XRD patterns, EDS, EA analysis, and crystal data and structure refinement parameters. CCDC 2282056–2282058. For ESI and crystallographic data in CIF or other electronic format see DOI: https://doi.org/10.1039/d3qi01439h

This journal is © the Partner Organisations 2023

Published on 15 9 2023. Downloaded on 2025-11-07 2:44:00.

dicular to the layers. The most popular 2D chalcogenide frameworks are layered tin chalcogenide frameworks (LTCFs), which are generally composed of Sn_3X_4 (X = S or Se) SBUs with various combinations of local coordination geometries of tin and sulfur (four, five and six coordinations for tin; two and three coordinations for sulfur). Interestingly, LTCFs have plain compositions but exhibit multifarious structural assemblies. The differences between the structures are mainly due to the linking modes between the adjacent clusters (*e.g.* single-corner Sn atoms, sharing Sn_2X_2 rings, Sn_2X_3 rings, Sn_3X_4 double rings, single-metal atom bridges and other complex linkers), the number of nodes in the ring (four/six/eight/ten-member rings), the packing mode of adjacent layers (*e.g.* A–B packing mode, A–B–C packing mode, and A–B–C–D packing mode), and the twist of the rings (elongated or compressed rings).[20,22,27–34] Till date, numerous 2D tin chalcogenide frameworks have been reported. Besides the effort for enriching the family of LTCFs, the exploration of potential applications was also carried out. By means of the porous structure and the "soft" skeleton, LTCFs exhibit excellent uptake efficiency for radionuclides (*e.g.*, radio-iodine, radio-cesium, radio-strontium, and radio-uranium) and rare earth elements (*e.g.*, lanthanum, terbium, and europium).[35–40] The intrinsic semiconducting property endows LTCFs with good photocatalytic activities.[21] In addition, the remarkable thermochromic property of LTCFs was also discussed using tin selenide frameworks.[41,42]

Obviously, LTCF semiconductors with multifarious architectures and high structural stability can be potential candidates for photoelectrochemistry, catalysis and host–guest chemistry-related applications. An in-depth study of the "structure–function" correlations in these fields is also accessible and meaningful. Although a large amount of LTCFs have been obtained, research on the systematic regulation of the structure of LTCFs is quit limited, and the investigation on photoelectrochemical property variation along with slight alteration of structures has never been reported. Herein, we report an example of "structure–property" correlations in the photoelectrochemical field by using three-layered tin chalcogenide frameworks, which show nuances in structural designs *via* the synergistic control of super base templates and auxiliary solvents. All of the three LTCFs (denoted as LTCF-1, LTCF-2 and LTCF-3) with the formula of $[Sn_3S_7]^{2-}\cdot 2HR$ (R = $C_7H_{12}N_2$ or $C_9H_{16}N_2$) have the same secondary building block (Sn_3S_4), linkers (shared Sn_2S_2) and 2D honeycomb-type topology. The slight difference is derived from the stacking and distortion of the layers, and the mean distance between adjacent clusters. LTCF-1 has interlaced stacking of the smooth layers leaving ignorable channels from the *c*-axis, while LTCF-2 and LTCF-3 adopt almost anastomotic stacking of the twisty layers, showing an obvious hexagonal channel perpendicular to the layer. The order according to the mean distance between the adjacent clusters from longest to shortest is LTCF-3, LTCF-1 and then LTCF-2. As a result, the three LTCFs exhibit distinct photoelectrochemistry performances that depend on the inconspicuous changes in structure.

Experimental section

Materials

Tin oxide (SnO_2, 99%, powder), tin (Sn, 99%, powder), sulfur (S, 99%, powder), 1,5-diazabicyclo[4.3.0]non-5-ene (DBN, 98%, liquid), 1,8-diazabicyclo[5.4.0]-7-undecene (DBU, >99%, liquid), *N*,*N*-dimethylformamide (DMF, >99.8%, liquid), hydrochloric acid solution (HCl, 12 M), sodium hydroxide (NaOH, 98%), sodium sulfate (Na_2SO_4, 98%, powder) and deionized water were all used without further purification.

Synthetic process

Preparation of LTCF-1. A mixture of tin oxide powder (30 mg), sulfur powder (120 mg), DBN (1 mL), DMF (1 mL) and deionized water (1 mL) was placed into a 23 mL Teflon-lined stainless-steel autoclave. After stirring for 20 min at room temperature, the reactor was sealed and heated in a blast air oven at 180 °C for 6 days. The autoclave was subsequently allowed to cool to room temperature, and about 80 mg colourless plate-like crystals of LTCF-1 were obtained.

Preparation of LTCF-2. A mixture of tin powder (60 mg), sulfur powder (60 mg), DBN (3 mL) and DMF (1 mL) was placed into a 23 mL Teflon-lined stainless-steel autoclave. After stirring for 20 min at room temperature, the reactor was sealed and heated in a blast air oven at 180 °C for 6 days. The autoclave was subsequently allowed to cool to room temperature, and about 150 mg colourless plate-like crystals of LTCF-2 were obtained.

Preparation of LTCF-3. A mixture of tin powder (60 mg), sulfur powder (120 mg), DBU (3 mL) and DMF (1 mL) was placed into a 23 mL Teflon-lined stainless-steel autoclave. After stirring for 20 min at room temperature, the reactor was sealed and heated in a blast air oven at 180 °C for 6 days. The autoclave was subsequently allowed to cool to room temperature, and about 200 mg colourless plate-like crystals of LTCF-3 were obtained.

Structural characterization

Single-crystal X-ray diffraction for LTCFs was performed using a Bruker SMART-1000 CCD diffractometer with graphite-monochromated Mo-Kα (λ = 0.71073 Å) radiation at room temperature. Absorption corrections on the three compounds were performed using the multi-scan program in APEX3. The structure was solved by a direct method using SHELXS-2014, and refinement against all reflections of the compounds was performed using SHELXL-2014. Solvent molecules were removed from the data set using the SQUEEZE routine of PLATON and refined further using the data generated. The powder X-ray diffraction (PXRD) data were collected using a SmartLab 9 diffractometer with Cu-Kα (λ = 1.54056 Å) radiation at room temperature. Energy-dispersive spectroscopic (EDS) analysis was performed using a scanning electron microscope (SEM) equipped with an EDS detector. An accelerating voltage of 25 kV and 40 s accumulation time were applied. Elemental analysis (EA) of C, H and N was performed using a VARIDEL III elemental analy-

Published on 15 9 2023. Downloaded on 2025-11-07 2:44:00.

zer. The samples were heated at 40 °C for 1 h before measurement.

UV-Vis absorption measurements

Room-temperature solid-state UV-vis diffusion reflectance spectra of the crystal samples were recorded using a SHIMADZU UV-3600 UV-Vis-NIR spectrophotometer, with a $BaSO_4$ powder as the reflectance reference. The absorption spectra were recorded from the reflectance spectra using the Kubelka–Munk function: $F(R) = \alpha/S = (1 - R)^2/2R$, where R, α, and S are the reflection, absorption, and scattering coefficient, respectively.

Photoelectrochemical measurements

First, 2 mg of the as-synthesized polycrystals were ground into a fine powder and then added into 200 μL of 0.5% Nafion. After ultrasonic treatment for 10 minutes, the obtained suspensions were dropped onto the surface of an ITO substrate and then dried at room temperature. The photocurrent experiments were performed using a CHI760E electrochemistry workstation in a three-electrode electrochemical cell, with a sample-coated ITO glass (effective area is around 1 cm^2) as the working electrode, a Pt wire as the auxiliary electrode, a saturated calomel electrode (SCE) as the reference electrode, and a sodium sulfate aqueous solution (0.5 M, 100 mL) as the supporting electrolyte. The light source is a 150 W high-pressure xenon lamp, located 20 cm away from the surface of the ITO electrode.

Surface photovoltage (SPV) measurements

SPV measurements were carried out on a grounded LTCF powder using a system that includes a lock-in amplifier (SR830-DSP) with a light chopper (SR540), a source of monochromatic light, a photovoltaic cell, and a computer. Monochromatic light was provided by a 500 W xenon lamp (CHFXQ500 W, Global Xenon Lamp Power) and a double-prism monochromator (Zolix SBP500). The contact between samples and the electrode of fluorine-doped tin oxide (FTO) was resistance free in measurements of SPV. The configuration of the photovoltaic cell is a sandwich-like structure of FTO–sample–FTO.

Results and discussion

The synthesis of three LTCFs was carried out under the perception deduced from previous synthetic experience that the combination of tin and sulfur prefers to result in a low-dimensional structure with small non-tetrahedral clusters rather than regular supertetrahedral clusters as secondary building blocks.[19,43] Tri/tetra-coordinated sulfur atoms in supertetrahedral clusters cannot apply enough negative charge to the surrounding high valence tin atoms. The best scheme is high-coordination tin surrounded by low-coordination sulfur, as in the most common Sn_3S_4 cluster, to realize the local charge balance. To create the nuance in foreseeable structures, the synergetic control of metallic precursors, organic super base (also served as a template) and auxiliary solvents was implemented in the solvothermal synthesis process. LTCF-1 was synthesized by using tin oxide as the metallic precursor, DBN as the structure-directing agent and the mixture of DMF/water as auxiliary solvents. When using DMF as an auxiliary solvent and substituting tin powder for tin oxide, LTCF-2 can be obtained. The synthetic strategy for LTCF-3 is similar to that of LTCF-2 except for the difference in the structure-directing agent, in which DBN is replaced by DBU. Single-crystal X-ray diffraction (SCXRD) analysis revealed that the LTCF-1 crystallized in a trigonal system with the space group $R\bar{3}$, while both LTCF-2 and 3 crystallized in a monoclinic system with the space group $P21/c$ (Table S1†). All of the three 2D compounds were composed of Sn_3S_4 clusters and bridged through shared Sn_2S_2 linkers. The interspace among the layers is occupied by protonated organic amine molecules, which cannot be identified due to their disorder. The experimental PXRD patterns of three compounds match well with their simulated ones, suggesting the validity of structures from the SCXRD data and phase purity of the as-synthesized powders (Fig. S1†). Scanning electron microscopic (SEM) images of the three LTCFs show their plate-like crystals with incised triangle morphology (LTCF-1), elongated hexagon morphology (LTCF-2) and regular hexagon morphology (LTCF-3), respectively, corresponding to the microcosmic layered packing model and discrepant structure. EDS and EA elemental analyses for Sn/S and C/H/N match well with the SCXRD results, indicating that the atoms in the framework of all these compounds are unambiguously determined (Fig. S2 and Table S2†).

Intralayer structure analysis

The nuance of the layers among the three LTCFs is mainly attributed to the flexible length and angle of the Sn–S bonds in clusters and linkers. The length of Sn–S bonds in three structures has a wide range from 2.344 Å to 2.739 Å (measured between atomic centers). Generally, six bonds at the edge of the cluster are comparable in length (about 2.46 Å on average), and obviously shorter than the three bonds at the centre of the cluster (about 2.64 Å on average), as the longer bond length at the centre can reduce the overburdened negative charge from the central sulfur atom to surrounded tin atoms according to the local charge balance rule and Brown's model calculation. There is also a significant difference in bond length among the linkers, which can range from 2.344 Å to 2.626 Å. The great difference can even emerge in a four-membered ring linker. For example, the shortest bond in the four-membered ring linker of Sn2–S2–Sn6–S1 in LTCF-2 is about 2.366 Å, while the longest one reaches 2.602 Å. This would be responsible for the different levels of distortion of the layers perpendicular to the c-axis. The linker bonds in LTCF-1 are rhythmically configured, in which the longer bonds with a length of about 2.5 Å and the shorter bonds with a length of about 2.4 Å alternately connect giving an approximately regular rhombus (Fig. S3†). However, the combinations of linker bonds in LTCF-2 and LTCF-3 are quite chaotic, leading to diversified orientations of linkers per-

 This journal is © the Partner Organisations 2023

Published on 15 9 2023. Downloaded on 2025-11-07 2:44:00.

pendicular to the *c*-axis. As a result, LTCF-1 exhibits a flat layer while both of LTCF-2 and LTCF-3 exhibit a waved layer (Fig. S4†).

The curvature of the linker in the *ab*-plane is also different among the three structures, which contributes to the distortion of the six-membered rings (regarding the Sn_3S_4 cluster as the node) and then layers in the *ab*-plane. LTCF-1 was constructed using two kinds of rings denoted as ring A and B respectively. Each orthohexagonal ring B is surrounded by six twisty hexagonal ring A, giving a pinwheel-shaped pattern (Fig. 1a). To better understand the arrangement of rings, a four-ring combination including three ring A and one ring B can be viewed as a higher hierarchical SBU and the layered structure of LTCF-1 is obtained through translational movement of this super unit. LTCF-2 and 3 have similar arrangements of rings and both the compounds are constructed using a single kind of six-membered ring. LTCF-2 was constructed using a twisty hexagonal ring C and its rollover ring C′ (obtained by rolling C along the *b*-axis with 180°) (Fig. 1b), and LTCF-3 constructed was using a slight twisty hexagonal ring D and its rollover ring D′ (obtained by rolling D along the *b*-axis with 180° and then along the *a*-axis with 180°) (Fig. 1c).

Packing of the layers

The layers of LTCFs pack into a superlattice mainly *via* an electrostatic interaction between negative inorganic layers and interspace counterions. Although all the three LTCFs have the semblable 2D layer structure, the packing mode of the layer is different, especially for LTCF-1. LTCF-1 adopts a complex A–B–C–A mode, while both LTCF-2 and 3 adopt an A–B–A mode. In LTCF-1, three adjacent isostructural layers stack in a staggered arrangement and periodically extend along the *c*-axis (Fig. 1d). Such packing mode blocks the channels composed of a six-membered ring. By comparison, LTCF-2 and 3 exhibit obvious channels from the *c*-axis despite the slightly staggering adjacent layers. For LTCF-2, the arrangement of adjacent two layers can be viewed as obtained by translating one of the layers with a distance of a six-membered ring along the *b*-axis, so that in LTCF-2, the opposite of the ring C is always ring C′ (Fig. 1e). Different from LTCF-2, the mismatch of the adjacent two layers in LTCF-3 can be viewed as formed by rolling over one of the layers with 180° along the *a*-axis (Fig. 1f). The retained channels in LTCF-2 and 3 make their internal more accessible compared to LTCF-1, especially when considering the smaller interspace of the LTCF-1 between adjacent layers (Fig. S5†).

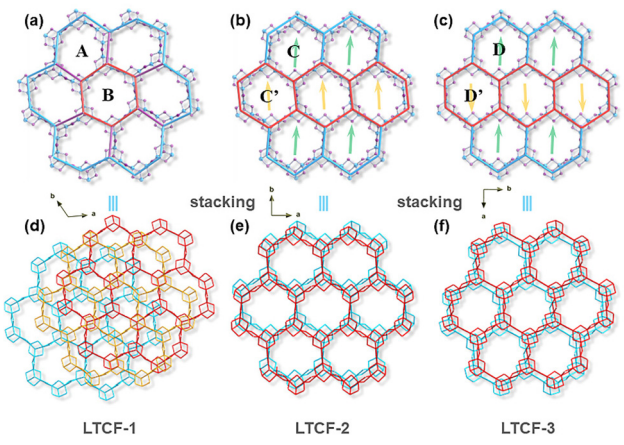

Fig. 1 Layer structure and stacking modes for LTCF-1 (a and d), LTCF-2 (b and e) and LTCF-3 (c and f). A–D represent the six-membered rings of LTCFs. C′ and D′ are rolling-over rings of C and D respectively. Green and yellow arrows represent pros and cons, and different orientation.

Photoelectrochemical and surface photovoltage performance

Photocurrent measurements on LTCFs were carried out to assess the effect of subtly modulating structures on the photo-induced carrier separation efficiency. The ground sample powder mixed with a Nafion solution was treated with ultrasound for sticking close to the ITO electrode. A Xe lamp without any cutoff filters was employed as the light source to simulate solar irradiation. Under the light irradiation, the photogenerated electrons and holes will separation and flow to the surface of the counter electrode and working electrode, with an applied potential promoting this process. The current–time (J–t) curves recorded at 0.6 V bias for LTCFs show an obvious photocurrent density difference. Among the three compounds, LTCF-3 exhibits a strong light-on photocurrent intensity, which is dramatically higher than that of LTCF-1 and almost five times as much as LTCF-2 (Fig. 2a). The current–time (J–t) results are further confirmed by the linear-sweep measurements. The linear-sweep curves for three LTCFs exhibit a similar tendency along the voltage variation under dark conditions. When the samples are irradiated by the light, the linear-sweep curve for LTCF-1 and 3 rises more rapidly than that for LTCF-2, and three curves reach the photoresponse density of 0.8 μA cm^{-2} (LTCF-1), 0.2 μA cm^{-2} (LTCF-2) and 1.1 μA cm^{-2} (LTCF-3) respectively at 0.6 V bias, which is consistent with the J–t results (Fig. 2b). The better photoelectric response performance suggests the higher efficiency of photo-induced charge separation. In addition, the photocurrent density for LTCF-1 and 3 decreases with a smooth curve after light-off, indicating the sluggish "electron–hole" recombination process, which is quite different from that of LTCF-2 (Fig. 2a and S6†).

SPV measurements were performed to assess the influence of charge separation efficiency on photovoltaic applications. The crystal powder of LTCFs were ground and then densified in the test cell. A 0.6 V bias was applied through top and bottom FTO electrodes. All the three LTCFs display obvious photovoltaic signals (Fig. S7†), which suggest that they are potentially used as intermediaries in solar-related applications. More importantly, LTCF-3 exhibits a stronger signal than that of LTCF-1 and LTCF-2, consistent with the photoelectric response results, indicating the important role of carrier separation in promoting the charge accumulation on the top electrode.

The efficiency of photo-induced charge separation mainly depends on the optical absorption ability from the thermodynamic aspect and the migration of the charge from the

Published on 15 9 2023. Downloaded on 2025-11-07 2:44:00.

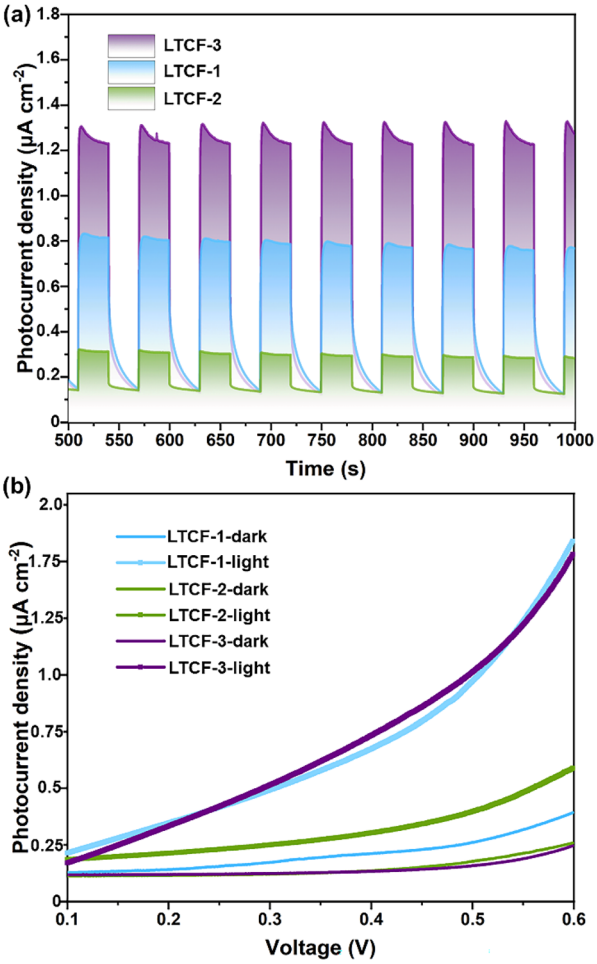

Fig. 2 Photoelectrochemical performance of three LTCFs. (a) Photoelectric response performance measured under 0.6 V bias. (b) LSV curves of LTCFs recorded under light and dark conditions.

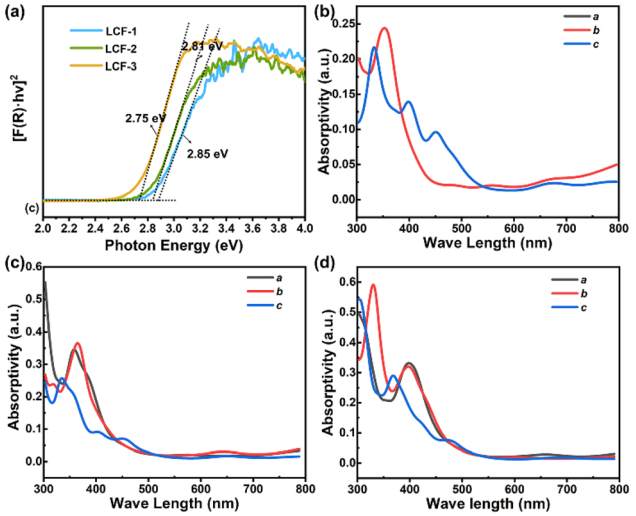

Fig. 3 Transformed Kubelka–Munk spectra of three LTCFs derived from the UV-vis diffuse reflection spectra (a). Theoretical calculations for the absorption property of LTCF-1 (b), LTCF-2 (c) and LTCF-3 (d) in *a*, *b*, or *c* direction.

dynamic aspect. Solid-state UV-vis absorption measurements were carried out to investigate the band gaps of LTCFs, by using the as-synthesized pure powder samples. Fig. 3a shows the transformed Kubelka–Munk spectra of three compounds. The band gaps of LTCF-1, LTCF-2 and LTCF-3 were determined to be about 2.85, 2.81 and 2.75 eV respectively, from the extrapolation of the linear part of spectra. As can be seen, three compounds have a close band gap, and the band gap of LTCF-2 falls between that of LTCF-1 and LTCF-3. Theoretical calculations for the absorption coefficient of the three compounds were carried out to further evaluate their optical absorption properties. The results show that all the three LTCFs have a coincident absorption peak position and a semblable absorption coefficient from the *c*-axis, in agreement with the similar layered structure (Fig. 3b–d). In addition, the optical absorption property of LTCF-2 from the *a*-axis and *b*-axis is similar to that of LTCF-3 from the *b*-axis and *a*-axis respectively, according to the absorption spectra of two structures. Although the absorption property of LTCF-1 from *a*/*b*-axis is slightly different to LTCF-2 and 3 in the *a*- or *b*-axis, due to the different packing of the layers in LTCF-1, the overall effect derived from small difference in absorption can be ignored. The UV-vis absorption performance and theoretical calculations suggest that it is the charge migration (closely related to the structure of the compound) rather than optical absorption leading to the discrepant photoelectric response.

Structurally, the interspace of the layers would impede the interaction among the layers, so that the intralayer charge migration dominates the dynamic process. It has been reported that in the hybrid cluster-based metal–chalcogenide frameworks, the photo-induced hot electrons inject into empty states in the cluster and can transfer between adjacent clusters through linkers.[5] Therefore, the recombined holes and hot electrons may come from different clusters, and a farther distance between adjacent clusters will reduce the probability of the hole–electron recombination derived from different clusters. The structure analysis shows that the mean distance between the adjacent clusters in LTCF-3 is about 3.6078 Å (measured between atomic centers of Sn in linker), obviously longer than 3.5208 Å in LTCF-1 and 3.5190 Å LTCF-2 (Fig. 4a–c). The inter-cluster charge transfer process in LTCF-3 is prolonged, contributing to the longer lifetime of carriers and higher photocurrent density (Fig. 4d). This inference is supported by the LSV performance of LTCFs. The LSV curves displayed in Fig. 2b show that all the three compounds have the closed photoelectric response intensity at 0.1 V bias. The response gap is enlarged upon increasing the bias. The carrier interaction among the adjacent clusters would first be strongly influenced because of the long migration distance under the external electric field. Therefore, the longer distance between adjacent clusters will result in a stronger photoelectric response signal when a high bias is applied.

This journal is © the Partner Organisations 2023

Published on 15 9 2023. Downloaded on 2025-11-07 2:44:00.

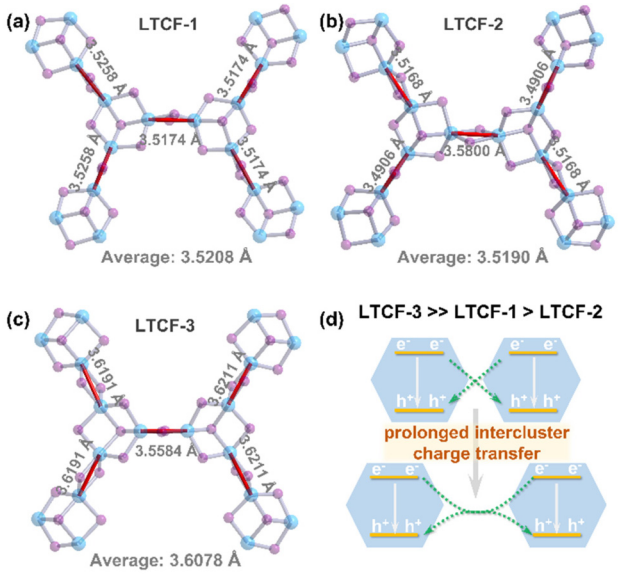

Fig. 4 Comparison between the three LTCFs in the distance between adjacent clusters (measured between Sn atomic center in linkers) (a–c). (d) Schematic diagram of intercluster charge transfer.

The band gap and the distribution of hot electrons were also analysed *via* theoretical calculations. The PDOS curves of LTCFs with the characteristic semiconducting features are shown in Fig. 5a. The band gaps obtained by PDOS analysis are consistent with the UV-vis absorption results. The major contribution of sulfur to the highest occupied molecular orbital (HOMO) and the obvious contribution of tin to the lowest unoccupied molecular orbital (LUMO) can also be inferred from the PDOS curves. More importantly, the distribution of the exited states near the LUMO on inorganic skeletons suggest that the hot electrons mainly gather in the region of clusters and can spread through the linkers, which may accelerate the recombination of the photo-induced carries (Fig. 5b).

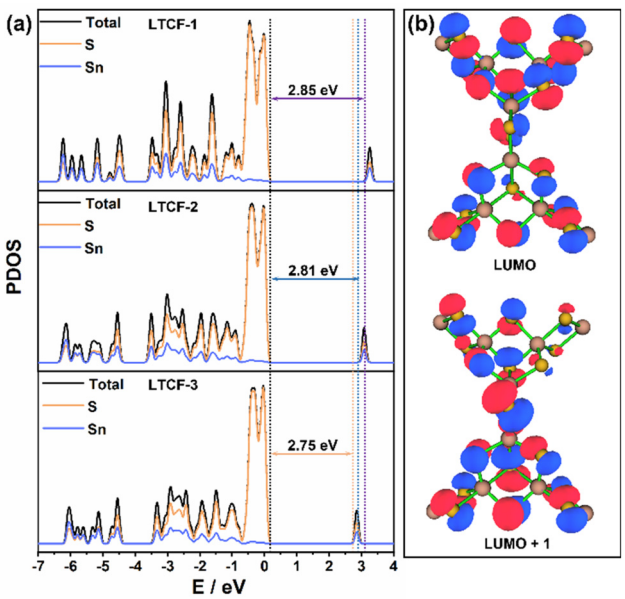

Fig. 5 Theoretical calculations for LTCFs. (a) Theoretical band gaps calculated from DOS curves. (b) Distribution of excited states around LOMO in the structure of LTCFs.

Conclusions

Three 2D tin chalcogenide frameworks with nuances in structures were obtained *via* subtle regulation in a solvothermal synthetic process. Among the three structures, LTCF-3 exhibits the best photoelectrochemical performance, which is dramatically higher than that of its isostructures LTCF-1 and LTCF-2. The charge transfer dynamics that depends on structure evolution was established by structure analysis, UV-vis absorption spectroscopy and theoretical calculations for three LTCFs. The enhanced photoelectric response for LTCF-3 is attributed to the longer distance between adjacent clusters, which would dramatically decrease the combination of photo-induced carriers. Such a "structure–property" correlation study represents an effective strategy for improving the photoelectrochemical performance of cluster-based inorganic semiconductors *via* optimizing the linkers or the distance of adjacent clusters.

Conflicts of interest

There are no conflicts to declare.

Acknowledgements

The authors acknowledge financial support from National Natural Science Foundation of China (22201117), Shandong Province Natural Science Foundation (ZR2022QB003), Doctoral Program of Liaocheng University (No. 318052049), Jiangsu Specially Appointed Professorship and the startup funding from Nanjing Normal University, and the Development Project of Youth Innovation Team in Shandong Colleges and Universities (2019KJC031).

References

1 X. Chen, X. Bu, Q. Lin, C. Mao, Q.-G. Zhai, Y. Wang and P. Feng, Selective Ion Exchange and Photocatalysis by Zeolite-Like Semiconducting Chalcogenide, *Chem. – Eur. J.*, 2017, **23**, 11913–11919.

2 D.-D. Hu, J. Lin, Q. Zhang, J.-N. Lu, X.-Y. Wang, Y.-W. Wang, F. Bu, L.-F. Ding, L. Wang and T. Wu, Multi-Step Host-Guest Energy Transfer Between Inorganic Chalcogenide-Based Semiconductor Zeolite Material and Organic Dye Molecules, *Chem. Mater.*, 2015, **27**, 4099–4104.

3 Y. Liu, J. Zhang, B. Han, X. Wang, Z. Wang, C. Xue, G. Bian, D. Hu, R. Zhou, D.-S. Li, Z. Wang, Z. Ouyang, M. Li and T. Wu, New Insights into Mn-Mn Coupling Interaction-

Published on 15 9 2023. Downloaded on 2025-11-07 2:44:00.

Directed Photoluminescence Quenching Mechanism in Mn^{2+}-Doped Semiconductors, *J. Am. Chem. Soc.*, 2020, **142**, 6649–6660.

4 W. Wang, H. Yang, C. Xue, M. Luo, J. Lin, D. Hu, X. Wang, Z. Lin and T. Wu, The First Observation on Dual Self-Closed and Extended Assembly Modes in Supertetrahedral T3 Cluster Based Open-Framework Chalcogenide, *Cryst. Growth Des.*, 2017, **17**, 2936–2940.

5 C. Xue, X. Fan, J. Zhang, D. Hu, X.-L. Wang, X. Wang, R. Zhou, H. Lin, Y. Li, D.-S. Li, X. Wei, D. Zheng, Y. Yang, K. Han and T. Wu, Direct observation of charge transfer between molecular heterojunctions based on inorganic semiconductor clusters, *Chem. Sci.*, 2020, **11**, 4085–4096.

6 H. Yang, M. Luo, L. Luo, H. Wang, D. Hu, J. Lin, X. Wang, Y. Wang, S. Wang, X. Bu, P. Feng and T. Wu, Highly Selective and Rapid Uptake of Radionuclide Cesium Based on Robust Zeolitic Chalcogenide via Stepwise Ion-Exchange Strategy, *Chem. Mater.*, 2016, **28**, 8774–8780.

7 P. Vaqueiro, S. Makin, Y. Tong and S. J. Ewing, A new class of hybrid super-supertetrahedral cluster and its assembly into a five-fold interpenetrating network, *Dalton Trans.*, 2017, **46**, 3816–3819.

8 P. Vaqueiro and M. L. Romero, Gallium-Sulfide Supertetrahedral Clusters as Building Blocks of Covalent Organic-Inorganic Networks, *J. Am. Chem. Soc.*, 2008, **130**, 9630–9631.

9 Y.-H. Wang, J.-B. Jiang, P. Wang, X.-L. Sun, Q.-Y. Zhu and J. Dai, Polymeric supertetrahedral InS clusters assembled by new linkages, *CrystEngComm*, 2013, **15**, 6040–6045.

10 C.-Y. Yue, X.-W. Lei, L.-J. Feng, C. Wang, Y.-P. Gong and X.-Y. Liu, $[Mn_2Ga_4Sn_4S_{20}]^{8-}$ T3 supertetrahedral nanocluster directed by a series of transition metal complexes, *Dalton Trans.*, 2015, **44**, 2416–2424.

11 N. Zheng, X. Bu and P. Feng, Nonaqueous Synthesis and Selective Crystallization of Gallium Sulfide Clusters into Three-Dimensional Photoluminescent Superlattices, *J. Am. Chem. Soc.*, 2003, **125**, 1138–1139.

12 X. Han, Z. Wang, D. Liu, J. Xu, Y. Liu and C. Wang, Co-assembly of a three-dimensional open framework sulfide with a novel linkage between an oxygen-encapsulated T3 cluster and a supertetrahedral T2 cluster, *Chem. Commun.*, 2014, **50**, 796–798.

13 H. Li, A. Laine, M. O'Keeffe and O. M. Yaghi, Supertetrahedral Sulfide Crystals with Giant Cavities and Channels, *Science*, 1999, **283**, 1145–1147.

14 Q. Lin, X. Bu, C. Mao, X. Zhao, K. Sasan and P. Feng, Mimicking High-Silica Zeolites: Highly Stable Germanium- and Tin-Rich Zeolite-Type Chalcogenides, *J. Am. Chem. Soc.*, 2015, **137**, 6184–6187.

15 J. Zhang, X. Wang, J. Lv, D.-S. Li and T. Wu, A multivalent mixed-metal strategy for single-Cu^{+}-ion-bridged cluster-based chalcogenide open frameworks for sensitive nonenzymatic detection of glucose, *Chem. Commun.*, 2019, **55**, 6357–6360.

16 X.-M. Zhang, D. Sarma, Y.-Q. Wu, L. Wang, Z.-X. Ning, F.-Q. Zhang and M. G. Kanatzidis, Open-Framework Oxysulfide Based on the Supertetrahedral $[In_4Sn_{16}O_{10}S_{34}]^{12-}$ Cluster and Efficient Sequestration of Heavy Metals, *J. Am. Chem. Soc.*, 2016, **138**, 5543–5546.

17 L. Zhang, C. Xue, W. Wang, D. Hu, J. Lv, D. Li and T. Wu, Stable Supersupertetrahedron with Infinite Order via the Assembly of Supertetrahedral T4 Zinc-Indium Sulfide Clusters, *Inorg. Chem.*, 2018, **57**, 10485–10488.

18 W. Wang, H. Yang, M. Luo, Y. Zhong, D. Xu, T. Wu and Z. Lin, A 36-Membered Ring Metal Chalcogenide with a Very Low Framework Density, *Inorg. Chem.*, 2017, **56**, 14730–14733.

19 C. Xue, D. Hu, Y. Zhang, H. Yang, X. Wang, W. Wang and T. Wu, Two Unique Crystalline Semiconductor Zeolite Analogues Based on Indium Selenide Clusters, *Inorg. Chem.*, 2017, **56**, 14763–14766.

20 T. Jiang and G. A. Ozin, New directions in tin sulfide materials chemistry, *J. Mater. Chem.*, 1998, **8**, 1099–1108.

21 J. Han, L. Zhang, S. Li, W. Zheng, D. Jia and Y. Yuan, Alcohol-solvothermal syntheses, crystal structures and photocatalytic properties of tin selenides with polyselenide ligands, *CrystEngComm*, 2019, **21**, 1642–1652.

22 D. Hu, Y. Zhang, H. Yang, J. Lin and T. Wu, Structural transformation of selenidostannates from 1D to 0D and 2D via a stepwise amine-templated assembly strategy, *Dalton Trans.*, 2017, **46**, 7534–7539.

23 M. J. Manos and M. G. Kanatzidis, Metal sulfide ion exchangers: superior sorbents for the capture of toxic and nuclear waste-related metal ions, *Chem. Sci.*, 2016, **7**, 4804–4824.

24 T. Wu, C. Xue, X. Bu and P. Feng, 5.10 - Crystalline inorganic materials from supertetrahedral chalcogenide clusters, in *Comprehensive Inorganic Chemistry III*, ed. J. Reedijk and K. R. Poeppelmeier, Elsevier, Oxford, 3rd edn, 2023, pp. 216–245.

25 Z. Wu, M. Luo, C. Xue, J. Zhang, J. Lv, X. Wang and T. Wu, New 2D Assemblage of Supertetrahedral Chalcogenide Clusters with Tetravalent-Metal-Induced Interrupted Sites, *Cryst. Growth Des.*, 2019, **19**, 4151–4156.

26 T. Yang, J.-M. Yu, L. Zhai, S. Jia, C. Yang, W.-W. Xiong and Q. Zhang, An inorganic-organic hybrid indium tin selenide featuring a two-dimensional layered structure for high efficient photocatalytic Cr(VI) reduction, *J. Cleaner Prod.*, 2023, **414**, 137643.

27 W.-W. Xiong, J. Miao, K. Ye, Y. Wang, B. Liu and Q. Zhang, Threading Chalcogenide Layers with Polymer Chains, *Angew. Chem., Int. Ed.*, 2015, **54**, 546–550.

28 C.-F. Du, N.-N. Shen, J.-R. Li, M.-T. Hao, Z. Wang and X.-Y. Huang, Synthesizing 2D and 3D Selenidostannates in Ionic Liquids: The Synergistic Structure-Directing Effects of Ionic Liquids and Metal-Amine Complexes, *Chem. – Asian J.*, 2016, **11**, 1555–1564.

29 T. Jiang, G. A. Ozin and R. L. Bedard, Nanoporous tin(IV) sulfides: Thermochemical properties, *Adv. Mater.*, 1995, **7**, 166–170.

30 J.-R. Li, W.-W. Xiong, Z.-L. Xie, C.-F. Du, G.-D. Zou and X.-Y. Huang, From selenidostannates to silver-selenidostan-

 This journal is © the Partner Organisations 2023

Published on 15 9 2023. Downloaded on 2025-11-07 2:44:00.

nate: structural variation of chalcogenidometallates synthesized in ionic liquids, *Chem. Commun.*, 2013, **49**, 181–183.

31 Y. Lin, W. Massa and S. Dehnen, Controlling the Assembly of Chalcogenide Anions in Ionic Liquids: From Binary Ge/Se through Ternary Ge/Sn/Se to Binary Sn/Se Frameworks, *Chem. – Eur. J.*, 2012, **18**, 13427–13434.

32 Y. Lin, D. Xie, W. Massa, L. Mayrhofer, S. Lippert, B. Ewers, A. Chernikov, M. Koch and S. Dehnen, Changes in the Structural Dimensionality of Selenidostannates in Ionic Liquids: Formation, Structures, Stability, and Photoconductivity, *Chem. – Eur. J.*, 2013, **19**, 8806–8813.

33 C. Tang, F. Wang, J. Lu, D. Jia, W. Jiang and Y. Zhang, Novel One-, Two-, and Three-Dimensional Selenidostannates Templated by Iron(II) Complex Cation, *Inorg. Chem.*, 2014, **53**, 9267–9273.

34 Z. Wang, C.-F. Du, C.-C. Cheng, N.-N. Shen, J.-R. Li and X.-Y. Huang, Two new selenidostannates with a $[Sn_3Se_7]_n^{2n-}$ layer from the imidazolium-based ionic liquids: The role of $(Bzmim)^+$ and aggregated cation of $[(Emim)_3Cl]^{2+}$, *Inorg. Chem. Commun.*, 2016, **74**, 58–61.

35 M.-L. Feng, D. Sarma, X.-H. Qi, K.-Z. Du, X.-Y. Huang and M. G. Kanatzidis, Efficient Removal and Recovery of Uranium by a Layered Organic-Inorganic Hybrid Thiostannate, *J. Am. Chem. Soc.*, 2016, **138**, 12578–12585.

36 J. Li, J. Jin, Y. Zou, H. Sun, X. Zeng, X. Huang, M. Feng and M. G. Kanatzidis, Efficient Removal of Cs^+ and Sr^{2+} Ions by Granulous $(Me_2NH_2)_{4/3}(Me_3NH)_{2/3}Sn_3S_7{\cdot}1.25H_2O$/Polyacrylonitrile Composite, *ACS Appl. Mater. Interfaces*, 2021, **13**, 13434–13442.

37 X.-H. Qi, K.-Z. Du, M.-L. Feng, Y.-J. Gao, X.-Y. Huang and M. G. Kanatzidis, Layered $A_2Sn_3S_7{\cdot}1.25H_2O$ (A = Organic Cation) as Efficient Ion-Exchanger for Rare Earth Element Recovery, *J. Am. Chem. Soc.*, 2017, **139**, 4314–4317.

38 X.-H. Qi, K.-Z. Du, M.-L. Feng, J.-R. Li, C.-F. Du, B. Zhang and X.-Y. Huang, A two-dimensionally microporous thiostannate with superior Cs^+ and Sr^{2+} ion-exchange property, *J. Mater. Chem. A*, 2015, **3**, 5665–5673.

39 D. Sarma, C. D. Malliakas, K. S. Subrahmanyam, S. M. Islam and M. G. Kanatzidis, $K_{2x}Sn_{4-x}S_{8-x}$ (x = 0.65–1): a new metal sulfide for rapid and selective removal of Cs^+, Sr^{2+} and UO_2^{2+} ions, *Chem. Sci.*, 2016, **7**, 1121–1132.

40 Y. Zhang, L. He, T. Pan, J. Xie, F. Wu, X. Dong, X. Wang, L. Chen, S. Gong, W. Liu, L. Kang, J. Chen, L. Chen, L. Chen, Y. Han and S. Wang, Superior Iodine Uptake Capacity Enabled by an Open Metal-Sulfide Framework Composed of Three Types of Active Sites, *CCS Chem.*, 2023, **5**, 1540–1548.

41 K.-Y. Wang, D. Ding, S. Zhang, Y. Wang, W. Liu, S. Wang, S.-H. Wang, D. Liu and C. Wang, Preparation of thermochromic selenidostannates in deep eutectic solvents, *Chem. Commun.*, 2018, **54**, 4806–4809.

42 K.-Y. Wang, H.-W. Liu, S. Zhang, D. Ding, L. Cheng and C. Wang, Selenidostannates and a Silver Selenidostannate Synthesized in Deep Eutectic Solvents: Crystal Structures and Thermochromic Study, *Inorg. Chem.*, 2019, **58**, 2942–2953.

43 P. Feng, X. Bu and N. Zheng, The Interface Chemistry between Chalcogenide Clusters and Open Framework Chalcogenides, *Acc. Chem. Res.*, 2005, **38**, 293–303.